

# Experimental Investigation of Stub Resonators Built in Plasmonic Slot Waveguides

Solmaz Naghizadeh, Adeel Afridi, Ongun Arisev, Aziz Karaşahin and Şükrü Ekin Kocabaş *Member, IEEE*

**Abstract**—In this work, we focus on stub resonators embedded in plasmonic slot waveguides. The resonators have potential applications in optical interconnects and sensors. We fabricate the samples by electron beam lithography and lift-off. We use a scattering matrix based model to quantify the optical power output from the samples. We measure the properties of the resonators by coupling light in and out of the slot waveguides by optical antennas, making use of a cross-polarization based setup utilizing a supercontinuum source and a high numerical aperture objective lens operating in the telecom-wavelength range. Our model agrees well with the measured data. Further development on the stub resonators can be made by using the methods in this paper.

**Index Terms**—Nanophotonics, optical resonators, scattering parameters, antenna measurements

## I. INTRODUCTION

CURRENT microprocessors have hit a speed limit due to energy dissipation constraints. Most of the dissipation is on the electrical wires used to form the circuits. Optical interconnects offer a viable way to reduce energy consumption by eliminating the loss on electrical wires and by enabling high data rates over large distances with high density pathways [1]. Such an interconnect system requires a number of optoelectronic components such as waveguides, light sources, modulators and detectors. When these components are tightly integrated with the transistors, it becomes conceivable to transfer a bit at the sub-femtojoule level, surpassing electrical interconnects [1]. Nanophotonic devices that take advantage of the optical properties of metals can have deep subwavelength dimensions, and they can provide both optical and electrical connectivity at the same time [2]—these properties are very relevant for intimate integration with transistors.

There are a number of different plasmonic waveguide proposals, with different propagation lengths and mode sizes [2]. Of these proposals, the plasmonic slot waveguide [3] is a very promising candidate for integration. Free-space [4], [5] and fiber based [6] couplers, interference based optical logic gates [7], photodetectors [8], mode converters [9], [10], directional couplers [11], [12], modulators [13], [14] and

This work was supported by the Scientific and Technological Research Council of Turkey (TUBITAK) under Grant No: 112E247.

S. Naghizadeh was with the Department of Physics, Koç University, Sarıyer, Istanbul, TR34450 Turkey. A. Afridi, O. Arisev and Ş. E. Kocabaş are with the Department of Electrical and Electronics Engineering at Koç University (email: ekocabas@ku.edu.tr). A. Karaşahin is with the Department of Electrical and Computer Engineering at the University of Maryland, College Park MD 20742 USA.

Copyright (c) 2016 IEEE. Personal use of this material is permitted. However, permission to use this material for any other purposes must be obtained from the IEEE by sending a request to pubs-permissions@ieee.org.

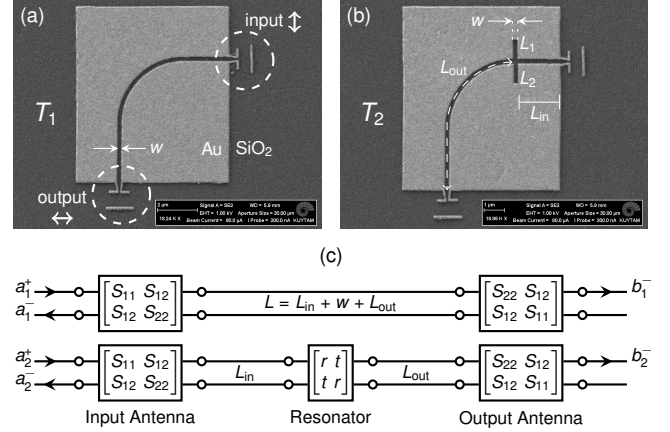


Fig. 1. SEM images of fabricated devices before SU8 coating for (a) samples without resonators, (b) samples with resonators. (c) Scattering matrix models for the devices.

light sources [15], [16] for the slot waveguide geometry have been demonstrated. The use of low-Q resonators that do not require active tuning can further improve the properties of light emitters, modulators and photodetectors without incurring an energy penalty [1]. Stub based resonators built in plasmonic slot waveguides can provide small mode volumes and be more compact compared to ring and Fabry-Perot counterparts [17]. Stub resonators have been experimentally investigated in U-shaped plasmonic channel waveguides [18] and in a hybrid plasmonic slot–photonic crystal waveguide geometry [19]. Straight, L- and T-shaped unconnected nanoslot resonator properties were experimentally probed in [20]. Recently, properties of 3D stub resonators based on plasmonic slot waveguides have been modeled using scattering matrix theory and verified via FDTD simulations [21]. In this letter, we experimentally investigate stub resonators built in plasmonic slot waveguides and compare measurements with the predictions of the model in [21].

## II. FABRICATION AND MODELING

Figure 1 shows the SEM images of the two types of samples used in the characterization of the stub resonators. We use gold (Au) as the metal layer and quartz (SiO<sub>2</sub>) as the substrate. We employ dipole antennas [11] to couple in and out of the slot waveguides. We build samples with no resonators in order to characterize the antenna–slot waveguide coupling rate and the modal properties of the slot waveguide [Fig. 1(a)]. We also build samples with double-stub resonators with stub lengths  $L_1$  and  $L_2$  embedded in the slot waveguide [Fig. 1(b)].

The slot width is fixed at  $w = 220$  nm and is also equal to the stub width. The distance between the resonator and the input (output) antenna is  $L_{\text{in}}$  ( $L_{\text{out}}$ ). Total length of the slot waveguide is the same in samples with and without resonators and is given by  $L = L_{\text{in}} + w + L_{\text{out}}$ .

The fabrication of the samples starts with spin coating of 4% in anisole 495K PMMA (Microchem) at 5000 rpm followed by 2% in anisole 950K PMMA at 5000 rpm to form a bi-layer resist on piranha cleaned quartz pieces. A thin (15 nm) aluminum layer is then evaporated to prevent the charging of the transparent substrate during e-beam lithography. A 100 kV e-beam lithography system (Vistec EBPG5000plusES) is operated at the 850–950  $\mu\text{C}/\text{cm}^2$  dose level. The aluminum layer is removed by a TMAH based developer (Microchem AZ 726). Standard PMMA development is made in 1:3 MIBK:IPA solution for 1 min. 4 nm of Ti and 115 nm of Au are thermally evaporated at  $2 \times 10^{-6}$  Torr pressure, at the rates 0.2  $\text{\AA}/\text{s}$  and 0.5  $\text{\AA}/\text{s}$ , respectively. These parameters have recently been found to be optimal for Au [22]. Lift-off procedure is done in heated ( $\sim 50$   $^\circ\text{C}$ ) acetone, as well as room temperature acetone with ultrasonic agitation. Finally, a  $\sim 500$  nm layer of SU8 2000 resist (Microchem) is coated on the samples to improve the coupling rate of the dipole antenna to the slot waveguide [6] and to increase the propagation length of the slot waveguide mode.

We use a scattering matrix based model in order to quantify the transmitted optical power from the samples in Fig. 1(a)-(b). The input and output antennas have the same structure, therefore, they use the same set of matrix elements [Fig. 1(c) top]. However, compared to the input antenna, the waveguide is on the opposite side of the output antenna which leads to the  $S_{11} \leftrightarrow S_{22}$  switch for the output antenna scattering matrix. The off-diagonal matrix elements are equal due to reciprocity. Samples with resonators have an additional scattering matrix composed of the reflection,  $r$ , and the transmission,  $t$ , coefficients of the double-stub resonator [Fig. 1(c) bottom].

The power transmission ratio of the devices without a resonator ( $T_1$ ) and those with a double-stub section ( $T_2$ ) can be estimated based on the scattering matrix model via  $T_i = |b_i^-/a_i^+|^2$  for  $i = 1, 2$  as shown in Fig. 1(c). In order to get closed form results for  $T_i$ , we convert the  $S$  matrix for each section in the model into the corresponding  $T$  matrix, multiply the  $T$  matrices to obtain the overall  $T$  matrix of the system (see e.g. [23]) and from the inverse of the upper-left element of the overall  $T$  matrix we arrive at

$$T_1 = |S_{12}^2 e^{-ikL} / (1 - S_{22}^2 e^{-i2kL})|^2, \quad (1)$$

$$T_2 = \left| \frac{t S_{12}^2 e^{-ikL^+}}{1 - S_{22}^2 (t^2 - r^2) e^{-i2kL^+} - 2r S_{22} \cos(kL^-) e^{-ikL^+}} \right|^2, \quad (2)$$

where  $L^\pm = L_{\text{in}} \pm L_{\text{out}}$ , and  $k$  is the wave vector of the plasmonic slot waveguide mode.

A thorough analysis of the  $r$  and  $t$  coefficients of the double-stub geometry, as well as the characterization of the slot waveguide mode and its  $k$  value are available in [21]. We obtain  $S_{12}$  and  $S_{22}$  from COMSOL simulations. When obtaining  $S_{12}$  we illuminate the antenna with a Gaussian beam and calculate the modal coupling coefficient. For  $S_{22}$ ,

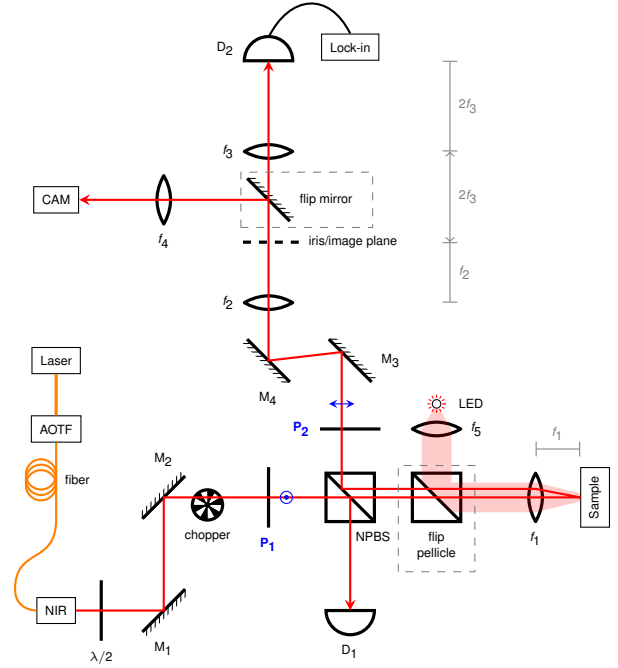


Fig. 2. Sketch of the optical measurement setup. Components enclosed in dashed rectangles are removed during measurements.

the waveguide mode is injected towards the antenna and the reflection is measured.

### III. OPTICAL MEASUREMENT SETUP

We use the cross-polarization based measurement method introduced in [4] to characterize the samples. The dipole antennas emit and receive light in a linearly polarized manner. We shine laser light polarized parallel to the input antenna and collect the light from the output antenna which is rotated  $90^\circ$  with respect to the input antenna [Fig. 1(a)]. We suppress the leakage from the input to the output through the use of a crossed polarizer in the output beam path, hence increase the signal-to-noise ratio. We borrow the dipole antenna design from [11] and use a radius of curvature of 3  $\mu\text{m}$  for the  $90^\circ$  bends with negligible radiation loss [11].

The sketch of the optical setup used in the measurements is provided in Fig. 2. Our setup is a modified version of the ones used in [4], [11], [14], primarily due to the lack of an infrared InGaAs CCD camera. We use a vidicon infrared camera Electrophysics Micronviewer 7290A (CAM) to locate the samples and align the laser beam to the input antenna. We then use a single pixel, 2 mm diameter Thorlabs DET20C InGaAs detector ( $D_2$ ) to measure the light from the output antenna. We also use a Thorlabs S122C Ge detector ( $D_1$ ) to account for any fluctuations in the laser power level.

We use a supercontinuum source (Fianium SC 450-4) connected to an acousto-optic tunable filter (AOTF) to get laser light in the 1200–1700 nm wavelength range. The AOTF has a long-pass filter installed before its fiber output (Thorlabs FELH1000). Two mirrors ( $M_{1,2}$ ) are used to align the laser beam to the high NA microscope objective lens (Leica HC PL FLUOTAR 100x/0.90 POL) with  $f_1 = 2$  mm, used to

focus light onto the input antenna. The polarizer  $P_1$  (Thorlabs LPNIR050-MP2) is set parallel to the input antenna whereas  $P_2$  is set parallel to the output antenna. A Thorlabs BS015 non-polarizing beam splitter (NPBS) is used to ensure that the polarization state of the light from the output antenna is preserved. An achromatic doublet (Thorlabs AC254-200-C) with  $f_2 = 200$  mm is used to form an intermediary image plane where magnification is  $f_2/f_1 = 100$ . Mirrors  $M_{3,4}$  position the light from the output antenna at the center of the intermediary image plane, and an iris is used to filter out all the light except that from the output antenna. We used a removable reticle (Thorlabs R1DS2P) at the image plane to help with the alignment. Another achromatic doublet (Thorlabs AC254-100-C) with  $f_3 = 100$  mm is used to relay the image to  $D_2$ . Similarly, the lens with  $f_4 = 75$  mm (Thorlabs AC254-075-C) is used to get an overall 150–200x magnification at the camera. A 3W red LED (Edison ES S1) is used to illuminate the sample surface with the help of a pellicle beam splitter.

Our measurement protocol is as follows. We mount the sample on a piezo stage (Thorlabs NanoMax-TS) with pitch and roll control (Thorlabs APR001) and make sure that the sample surface is perpendicular to the laser beam. We set the wavelength to 1550 nm, rotate the Thorlabs AHW05M-1600 half-wave plate ( $\lambda/2$ ) and maximize the power through  $P_1$ . We set  $P_2 \parallel P_1$ , and focus the laser light on the quartz substrate by minimizing the beam width via adjusting the sample distance to the objective lens by the piezo controller. We then set  $P_2 \perp P_1$  and observe the formation of the clover pattern on quartz, typical of Gaussian beams when focused by a high NA objective [11]. We move the clover pattern over the input antenna, observe some light from the output antenna, use the iris to block the clover pattern and get light only from the output antenna. We turn-off the LED, remove the pellicle, switch to  $D_2$ , and get a reading from the lock-in amplifier (SRS SR830). We maximize the lock-in reading by moving the sample via the piezo controller in the plane perpendicular to the laser light, without changing the sample to objective lens distance. We then scan the wavelength and record  $D_{1,2}$  readings.

#### IV. RESULTS, DISCUSSION AND CONCLUSION

We characterized a number of different samples with and without resonators. Fig. 3(a) shows the captured camera image<sup>1</sup> for a double-stub resonator sample when the stub is resonant and has a large  $|r|$  [equivalently  $|t|$  is near its minimum, see dashed line in Fig. 4(c)]. There is considerable leakage from the stub section, and the antenna output intensity is quite low, as highlighted by the white-dashed circle. On the other hand, when the wavelength moves away from the stub resonance and  $|t|$  increases, leakage from the stub decreases and the antenna output becomes more pronounced [Fig. 3(b)].

We show the results for the power transmission through waveguides without stub resonators ( $T_1$ ) in Fig. 4(a). We normalize the experimental curves with an estimate of the

<sup>1</sup>The fact that the illumination LED is at  $\sim 630$  nm and the laser light is at 1325 nm leads to a small shift and defocus of the sample image on the camera with respect to the laser beams due to the chromatic aberrations in the system.

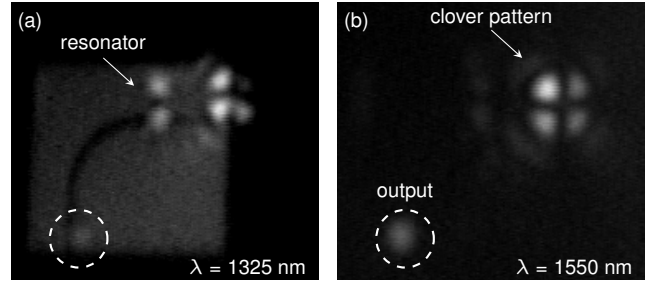


Fig. 3. A double-stub resonator sample with stub lengths  $L_1 = L_2 = 0.98 \mu\text{m}$  (a) excited at  $\lambda = 1325$  nm and imaged with the LED light on. (b) The same sample excited at  $\lambda = 1550$  nm and imaged without LED lighting and with the pellicle removed.

incident power which is obtained by measuring the reflection of laser light from a large metal patch on the sample while  $P_2 \parallel P_1$ . We obtain data from nine different samples, similar to Fig. 1(a), with a total waveguide length  $L = 12 \mu\text{m}$ . Although the nine samples had exactly the same e-beam mask, due to variations during the fabrication, we see variations in  $T_1$ . We average over the measurements to obtain the thick red line in Fig. 4(a). We also calculate  $T_1$  via (1), where in  $S_{12}$  simulations we take into account the changes in the Gaussian beam width and center position as the wavelength is scanned (measured experimentally from camera images of the beam reflecting off of a blank quartz section on the sample). We normalize the calculated  $T_1$  (black curve) so that it has the same maximum value as the average measurement results (red curve). The fringes in  $T_1$  are due to the low-Q cavity formed by the antennas and the  $L = 12 \mu\text{m}$  waveguide. As reported in [8] the fringe spacing and depth can be used to obtain the real and imaginary parts of  $k$ , respectively. The calculated  $k$  values correctly gave us the fringe spacing which is a function of the real part of  $k$ ; to match the fringe depths, we had to increase the imaginary part of  $k$  by 50% to give us a power transmission length,  $\frac{1}{2\text{Im}(k)}$ , of  $5.3 \mu\text{m}$  for the waveguide mode at 1550 nm. We get very good correspondence between the measurements and the model around 1550 nm, the wavelength at which we focus our laser beam. The correspondence deteriorates at lower and higher wavelengths, probably due to the non-orthogonality of the sample surface to the laser beam and chromatic aberrations.

We measure the power transmitted through samples with stub resonators ( $T_2$ ) for three different sets of stub lengths ( $L_{1,2}$ ) from samples similar to Fig. 1(b). We plot measurement results for  $T_2/T_1$  for each  $L_{1,2}$  set in Fig. 4(b–d) where  $T_1$  is taken to be the average measurement in Fig. 4(a). In each subplot, we have three different samples with the same e-beam mask dimensions (thin pink lines) with variations in the measurements due to fabrication. We plot the average of the experimental measurements with thick red lines. We also plot calculated  $T_2/T_1$  from (1)–(2) (thick black lines) and calculated  $|t|^2$  from [21] (black dashed lines). The e-beam mask dimensions for the stubs were  $L_{1,2} = 1380$  nm for Fig. 4(b),  $L_{1,2} = 910$  nm for Fig. 4(c), and  $L_1 = 430, L_2 = 910$  nm for Fig. 4(d). These values were chosen to have a transmission maximum at 1550 nm [21]. However, we had longer stubs

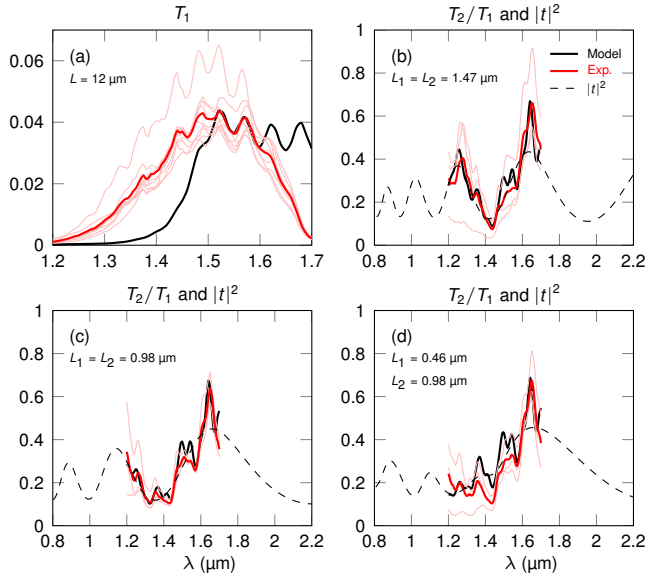


Fig. 4. (a) Transmission measurements from nine samples without a resonator (thin pink), their average (thick red) and the estimate from (1) (thick black). (b–d) Transmission from samples with resonators for three different sets of  $L_{1,2}$  normalized by  $T_1$ , from experimental measurements (thin pink), their average (thick red), estimate from (1)–(2) (thick black) and plot of  $|t|^2$  (dashed). Fitted  $L_{1,2}$  values are shown in (b–d).

in the fabricated samples as observed from SEM images, and the resonators were all resonant at 1650 nm. We fitted  $L_{1,2}$  values so that the experimental  $T_2/T_1$  values and those calculated via (1)–(2) agree well with each other. In (1)–(2) we use the  $k$  values obtained from Fig. 4(a). The fitted values of  $L_{1,2}$  reported in Fig. 4(b–d) are  $\sim 6\%$  larger than those on the e-beam mask. The fitted values are also used in the calculation of  $|t|^2$ . As can be seen, there is a good overlap between the predictions of the scattering matrix model and the experimental data. Furthermore, we see that  $T_2/T_1$  follows  $|t|^2$ , with extra ripples due to the low-Q resonances set up in between the two antennas and the connecting waveguide.

In conclusion, we experimentally characterized stub resonators embedded in plasmonic slot waveguides. We used the scattering matrix based characterization of the resonators in an extended model which takes into account the coupling of a Gaussian beam into the slot waveguide mode by an optical antenna. We provided details of the optical characterization setup and have shown that the measurements and modeling agree with each other. Our results are also relevant for stub designs at THz frequencies [24]. The development of compact resonators embedded in plasmonic slot waveguides can pave the way to sensors with an improved figure of merit as well as detectors with very low energy consumption.

## REFERENCES

- [1] D. A. B. Miller, “Attojoule optoelectronics for low-energy information processing and communications – a tutorial review,” *Journal of Lightwave Technology*, vol. PP, no. 99, pp. 1–1, 2017, (early access).
- [2] N. Kinsey, M. Ferrera, V. M. Shalaev, and A. Boltasseva, “Examining nanophotonics for integrated hybrid systems: a review of plasmonic interconnects and modulators using traditional and alternative materials,” *J. Opt. Soc. Am. B*, vol. 32, no. 1, pp. 121–142, Jan 2015.

- [3] G. Veronis and S. H. Fan, “Modes of subwavelength plasmonic slot waveguides,” *Journal of Lightwave Technology*, vol. 25, no. 9, pp. 2511–2521, September 2007.
- [4] J. Wen, P. Banzer, A. Kriesch, D. Ploss, B. Schmauss, and U. Peschel, “Experimental cross-polarization detection of coupling far-field light to highly confined plasmonic gap modes via nanoantennas,” *Applied Physics Letters*, vol. 98, no. 10, p. 101109, 2011.
- [5] A. Andryieuski, V. A. Zenin, R. Malureanu, V. S. Volkov, S. I. Bozhevolnyi, and A. V. Lavrinenko, “Direct characterization of plasmonic slot waveguides and nanocouplers,” *Nano Lett.*, vol. 14, no. 7, pp. 3925–3929, Jul. 2014.
- [6] Q. Gao, F. Ren, and A. X. Wang, “Direct and efficient optical coupling into plasmonic integrated circuits from optical fibers,” *IEEE Photonics Technology Letters*, vol. 28, no. 11, pp. 1165–1168, June 2016.
- [7] Y. Fu, X. Hu, C. Lu, S. Yue, H. Yang, and Q. Gong, “All-optical logic gates based on nanoscale plasmonic slot waveguides,” *Nano Letters*, vol. 12, no. 11, pp. 5784–5790, 2012.
- [8] D.-S. Ly-Gagnon, K. C. Balram, J. S. White, P. Wahl, M. L. Brongersma, and D. A. B. Miller, “Routing and photodetection in subwavelength plasmonic slot waveguides,” *Nanophotonics*, vol. 1, no. 1, pp. 9–16, 2012.
- [9] P. Geisler, G. Razinskas, E. Krauss, X.-F. Wu, C. Rewitz, P. Tuchscherer, S. Goetz, C.-B. Huang, T. Brixner, and B. Hecht, “Multimode plasmon excitation and *In Situ* analysis in top-down fabricated nanocircuits,” *Phys. Rev. Lett.*, vol. 111, p. 183901, Oct 2013.
- [10] W.-H. Dai, F.-C. Lin, C.-B. Huang, and J.-S. Huang, “Mode conversion in high-definition plasmonic optical nanocircuits,” *Nano Lett.*, vol. 14, no. 7, pp. 3881–3886, Jul. 2014.
- [11] A. Kriesch, S. P. Burgos, D. Ploss, H. Pfeifer, H. A. Atwater, and U. Peschel, “Functional plasmonic nanocircuits with low insertion and propagation losses,” *Nano Letters*, vol. 13, no. 9, pp. 4539–4545, 2013.
- [12] C. Rewitz, G. Razinskas, P. Geisler, E. Krauss, S. Goetz, M. Pawtowska, B. Hecht, and T. Brixner, “Coherent control of plasmon propagation in a nanocircuit,” *Phys. Rev. Applied*, vol. 1, p. 014007, Feb 2014.
- [13] A. Melikyan, L. Alloatti, A. Muslija, D. Hillerkuss, P. C. Schindler, J. Li, R. Palmer, D. Korn, S. Muehlbrandt, D. V. Thourhout, B. Chen, R. Dinu, M. Sommer, C. Koos, M. Kohl, W. Freude, and J. Leuthold, “High-speed plasmonic phase modulators,” *Nat Photon*, vol. 8, no. 3, pp. 229–233, Mar. 2014.
- [14] H. W. Lee, G. Papadakis, S. P. Burgos, K. Chander, A. Kriesch, R. Pala, U. Peschel, and H. A. Atwater, “Nanoscale conducting oxide PlasMOSTor,” *Nano Letters*, vol. 14, no. 11, pp. 6463–6468, 2014.
- [15] Y.-S. No, J.-H. Choi, H.-S. Ee, M.-S. Hwang, K.-Y. Jeong, E.-K. Lee, M.-K. Seo, S.-H. Kwon, and H.-G. Park, “A double-strip plasmonic waveguide coupled to an electrically driven nanowire LED,” *Nano Lett.*, vol. 13, no. 2, pp. 772–776, Feb. 2013.
- [16] K. C. Y. Huang, M.-K. Seo, T. Sarmiento, Y. Huo, J. S. Harris, and M. L. Brongersma, “Electrically driven subwavelength optical nanocircuits,” *Nat Photon*, vol. 8, no. 3, pp. 244–249, Mar. 2014.
- [17] S. I. Bozhevolnyi, V. S. Volkov, E. Devaux, J.-Y. Laluet, and T. W. Ebbesen, “Channel plasmon subwavelength waveguide components including interferometers and ring resonators,” *Nature*, vol. 440, no. 7083, pp. 508–511, Mar. 2006.
- [18] Y. Zhu, X. Hu, H. Yang, and Q. Gong, “On-chip plasmon-induced transparency based on plasmonic coupled nanocavities,” *Scientific Reports*, vol. 4, p. 3752, Jan. 2014.
- [19] Z. Chai, X. Hu, C. Li, H. Yang, and Q. Gong, “On-chip multiple electromagnetically induced transparencies in photon-plasmon composite nanocavities,” *ACS Photonics*, Oct. 2016.
- [20] S. Raza, M. Esfandyarpour, A. L. Koh, N. A. Mortensen, M. L. Brongersma, and S. I. Bozhevolnyi, “Electron energy-loss spectroscopy of branched gap plasmon resonators,” *Nature Communications*, vol. 7, p. 13790, Dec. 2016.
- [21] S. Naghizadeh and Şükrü Ekin Kocabaş, “Guidelines for designing 2D and 3D plasmonic stub resonators,” *J. Opt. Soc. Am. B*, vol. 34, no. 1, pp. 207–217, Jan 2017.
- [22] K. M. McPeak, S. V. Jayanti, S. J. P. Kress, S. Meyer, S. Iotti, A. Rossinelli, and D. J. Norris, “Plasmonic films can easily be better: Rules and recipes,” *ACS Photonics*, vol. 2, no. 3, pp. 326–333, 2015.
- [23] Ş. E. Kocabaş, G. Veronis, D. A. B. Miller, and S. Fan, “Transmission line and equivalent circuit models for plasmonic waveguide components,” *Selected Topics in Quantum Electronics, IEEE Journal of*, vol. 14, no. 6, pp. 1462–1472, Nov.-Dec. 2008.
- [24] J. Tao, B. Hu, X. Y. He, and Q. J. Wang, “Tunable subwavelength terahertz plasmonic stub waveguide filters,” *IEEE Transactions on Nanotechnology*, vol. 12, no. 6, pp. 1191–1197, Nov 2013.